JOURNAL OF CATALYSIS 115, 159–179 (1989)

Pillared-Clay Catalysts Containing Mixed-Metal Complexes

I. Preparation and Characterization

WOO Y. LEE,* RASIK H. RAYTHATHA,† AND BRUCE J. TATARCHUK*,[1]

*Department of Chemical Engineering, Auburn University, Auburn, Alabama 36849, and †ECC-America, P.O. Box 471, Sandersville, Georgia 31082

Received December 22, 1987; revised August 17, 1988

High-surface-area pillared clays were prepared from naturally occurring montmorillonites by exchanging interlayer ions with polyoxocations containing (i) iron, (ii) aluminum, (iii) discrete mixtures of (i) and (ii), or (iv) iron *and* aluminum located within the same complex. The valence state, solid-state properties, and stability of these pillars were determined following reduction and oxidation using Mössbauer spectroscopy, X-ray diffraction, and BET surface area measurements. Controlled atmosphere electron microscopy and transmission electron microscopy were also used to follow the nucleation and sintering behavior of the pillars during reduction. Mössbauer data suggested interlayer formation of metallic iron domains following reduction of types (i) and (iii) pillared systems. The magnetic properties and the oxidation behavior deduced from Mössbauer analysis and the complementary insights provided by XRD strongly indicated that these crystallites were in the form of thin-film/pancake-shape islands most likely conforming to the geometry of the interlayer region. Reduced domains remained accessible to the gas phase and in some cases resisted sintering during reduction/oxidation cycles. Reduction of the iron phase could be enhanced by addition of platinum to the sample. The absence of Mössbauer features attributable to Fe–Pt alloys and the onset of iron reduction, from Fe^{3+} to Fe^{2+}, at room temperature suggested that reduction was facilitated by hydrogen spillover from platinum. The expanded structures of types (ii) and (iii) pillared systems were found to be relatively stable following reduction up to 723 K due to the irreducible nature of discrete aluminum pillars under these conditions. At appropriate iron pillar to aluminum pillar ratios, results obtained from type (iii) pillared systems also indicated that at least one monolayer of Fe^{2+} was preferentially decorated/accommodated at the surfaces of the aluminum oxide pillars. This behavior was attributed to the relatively stronger interaction of iron with alumina than with silica and was triggered at temperatures ≤673 K by introducing platinum, and presumably hydrogen atoms, to the specimen. On the basis of the findings noted above, intercalation of clays with mixtures of chemically distinct pillars appears to provide a unique method for preparing highly dispersed metallic or even bimetallic catalysts possessing two-dimensional sieve-like behavior with high overall surface areas and high loadings of the active metal.

INTRODUCTION

Naturally occurring montmorillonite clays are layered alumino-silicates which, in their natural state, are held together by weak electrostatic forces. New classes of materials have recently been developed by exchanging the small Na^+ ions that are normally found between these layers with inorganic metal ions of larger size and charge (*1–3*). Subsequent freeze-drying or heating at ca. 473 K removes the solvent (i.e., water), leaving the alumino-silicate layers "propped apart" by the metal ions (i.e., pillars). The N_2 BET surface areas of these "pillared clays" typically increases from ca. 20 m^2/g before pillaring to greater than 250 m^2/g after this procedure. Inorganic polymeric metal ions derived from water-soluble salts of aluminum, iron, chromium, bismuth, magnesium, zirconium, cobalt, and nickel appear to be the most widely explored pillaring agents (*4*), although it has been reported that pillaring species derived

[1] To whom all correspondence should be addressed.

0021-9517/89 $3.00

from molybdenum, niobium, silicon, and other metal ions have also been prepared (*5–7*).

Microporous networks created in the interlayer region of clays after pillaring provide pore-size distributions of extended range (ca. 0.6 to 4.0 nm) compared to those found within typical zeolites (ca. 0.2 to 0.8 nm) (*8*). Clays intercalated with aluminum pillars, therefore, have been evaluated as potential catalysts for cracking large hydrocarbon molecules. Major difficulties exist, however, as these materials are relatively unstable at typical reaction and regeneration temperatures (*9*). Nevertheless, several studies (*7, 9, 10*) have shown that aluminum pillared clays are active cracking catalysts at milder temperatures (ca. 773 to 813 K) in laboratory scale experiments.

To date, clays intercalated with monometallic pillars have received primary attention. The present work, however, investigates pillared clays containing mixed-metal complexes. Discrete metal pillars of iron oxide and aluminum oxide are simultaneously intercalated into montmorillonite to produce "mixed pillared systems." Mixed pillared clays have been prepared to investigate whether they can serve as precursor materials for the synthesis of small iron crystallites during reduction. It is hoped that reduction-resistant aluminum oxide pillars may preserve the structure of the pillared clay in sufficient detail so that it can serve as a "jello mold" to facilitate the nucleation and growth of iron crystallites in the absence of sintering. If this process can be accomplished, pillared clays can then be used as high-surface-area metallic or bimetallic catalyst supports providing tight control of crystallite size along with the inherent shape selectivity dictated by the interlayer dimensions.

The objectives of the present study are, therefore, to (i) discern whether or not our preparation methods are capable of synthesizing mixed pillared clays containing discrete iron and aluminum pillars, (ii) study the reduction behavior of iron in the mixed pillared clays with emphasis on the synthesis of small iron crystallites, and (iii) determine the stability of the mixed pillared clays at elevated temperatures.

In order to accomplish these tasks, Mössbauer spectroscopy, XRD, N_2 BET surface area measurements, controlled atmosphere electron microscopy (CAEM) and transmission electron microscopy (TEM) have been used to investigate the reduction behavior and the structural properties of mixed pillared clays as a function of appropriate chemical treatments. Pillared clays containing monometallic pillars (i.e., iron and aluminum) and alloy pillars (i.e., iron and aluminum located in the same pillar) have also been investigated for comparative purposes to distinguish and ascertain the chemical integrity and the stability of the mixed pillared systems.

EXPERIMENTAL

Sample Preparation

Montmorillonite used in this work was a commercial product, Mineral Colloid B.P., obtained courtesy of Southern Clay Products. This material was saturated with sodium ions by stirring in 1 *M* sodium chloride for 24 h, washed with distilled water to remove excess salt, and freeze-dried. The cation exchange capacity (CEC) of the product was determined by reexchange of sodium ions with ammonium ions. The quantity of nitrogen in the ammonium-exchanged montmorillonite was determined by Galbraith Laboratories, Inc. The amount of nitrogen exchanged was corrected for the natural abundance of nitrogen in the clay. The cation exchange capacity was determined to be 82 meq/100 g of Na^+-saturated montmorillonite.

Iron pillaring agents, $[Fe_3(OH)_4]Cl_5$, enriched with ^{57}Fe, were prepared as follows: (i) a stock solution of $FeCl_3$ was prepared by dissolving 0.014 g of 93.7% ^{57}Fe-enriched ferric oxide (Isotope Division of Oak Ridge National Laboratory) in 2 ml of concentrated hydrochloric acid (12 *M*) at room temperature with subsequent dilution to 10 ml using distilled water; (ii) 1.230 g of unenriched ferric trichloride hexahydrate (Al-

drich) was dissolved in 75 ml of water; (iii) 1 ml of the ^{57}Fe-enriched solution was added slowly to the unenriched solution; (iv) a solution containing 0.608 g of sodium carbonate in 25 ml of water was slowly added to solution (iii) to neutralize excess HCl and provide an OH/M (hydroxyl to metal) ratio of 2.0; and (v) the resulting solution was aged at 368 K for 36 h. The ^{57}Fe enrichment in the final solution was 8.6%. Solutions of $[Fe_3(OH)_4]Cl_5$ with different ^{57}Fe enrichments were prepared using similar procedures.

An aluminum pillaring agent, $[Al_{13}O_4(OH)_{24}]Cl_7$, commercially known as Chlorohydrol, was purchased as a solution from Reheis Chemicals Co. with an active ingredient content of 50 wt%.

Alloy pillaring agents, $[Al_{12.5}Fe_{0.5}O_4(OH)_{24}]Cl_7$, containing mixtures of aluminum and iron in the ratio 12.5 : 0.5, respectively, were prepared as follows: (i) 5.568 g of aluminum trichloride hexahydrate (Aldrich) and 0.250 g of ferric trichloride hexahydrate were dissolved in 98 ml of water; (ii) 1.5 ml of the stock solution containing enriched ferric chloride was added and the resulting solution allowed to stand for 5 min; (iii) a solution containing 3.145 g of sodium carbonate in 50 ml of water was slowly added to neutralize excess hydrochloric acid and provide an OH/*M* ratio of 2.5; and (iv) the resulting solution was aged at 368 K for 36 h. The ^{57}Fe enrichment in the final solution was 63%.

Using the pillaring agents noted above, five different samples were prepared. These clays were intercalated with (i) only discrete aluminum pillars, "100 Al-PILC"; (ii) only discrete iron pillars, "100 Fe-PILC"; (iii) a mixture of discrete iron pillars and discrete aluminum pillars composing 75 and 25% of the CEC, respectively, "75/25 Fe/Al-PILC"; (iv) a mixture of discrete iron pillars and discrete aluminum pillars composing 50% each of the CED, "50/50 Fe/Al PILC"; and (v) alloy pillars with an Al/Fe stoichiometry of 12.5/0.5, respectively, "alloy-PILC."

The 100 Al-PILC was prepared according to procedures described by Pinnavaia and Raythatha (*11*). The amount of Chlorohydrol used was equivalent to four times the CEC of the montmorillonite. The resulting slurry was stirred at 338 K for 2 h, cooled, and washed repeatedly with distilled water to remove excess pillaring agent. These clays were then freeze-dried. This same procedure was also followed during preparation of 100 Fe-PILC and alloy-PILC except that $[Fe_3(OH)_4]Cl_5$ and $[Al_{12.5}Fe_{0.5}O_4(OH)_{24}]Cl_7$ stock solutions were used, respectively.

The preparation procedure for mixed pillared clays was nearly identical to that for 100 Al-PILC except that predetermined volumes of $[Fe_3(OH)_4]Cl_5$ and Chlorohydrol solutions were added to the montmorillonite slurry. Appropriate adjustments were made to account for the cationic charges of Chlorohydrol (i.e., 7+) and $[Fe_3(OH)_4]Cl_5$ (i.e., 5^+) when determining the volumes of the solutions needed to satisfy the aforementioned CEC specifications. The iron contents in the pillared-clay samples, as determined by Galbraith Laboratories, were also followed (*12*). Comparison between the measured iron loadings and those calculated assuming 100% replacement of the CEC by the appropriate species indicates that some minor discrepancies exist in the overall preparation procedure. At present the exact source(s) of these deviations is unclear but can potentially be attributed to a number of factors including (i) formation of somewhat larger polyoxocations with greater numbers of iron atoms per unit charge and (ii) precipitation/hydrolysis of some uncharged iron oxide species within the clay network during exchange (*12*).

Some clay samples (i.e., 100 Fe-PILC, 50/50 Fe/Al-PILC, and alloy-PILC) were also impregnated with ca. 1.0 wt% platinum using chloroplatinic acid (Alfa Products, 99.9% purity) and incipient wetness procedures.

Gases

Hydrogen (99.99%) and helium (99.99%) were obtained from Selox, Inc., and puri-

fied prior to reduction and BET studies by sequential passage through a Deoxo unit at 298 K, a copper turning trap at 500 K, and a bed of 13*X* zeolites at 77 K. Ultrapure oxygen (99.99%, Selox, Inc.) used for oxidation treatments was purified using 13X zeolites at 196 K. Nitrogen used for BET studies (99.99%, Selox, Inc.) was purified using a copper turning trap at 500 K and a bed of 13X zeolites at 77 K.

Mössbauer Spectroscopy

Transmission Mössbauer spectra were obtained in a constant acceleration mode using equipment and procedures described in detail elsewhere (*12*). Zero velocity was defined with respect to the centroid of the metallic iron spectrum and positive velocity was defined as the source approaching the absorber.

Pillared clays (ca. 0.30 g) were pressed into thin wafers having a diameter of 25.4 mm at a pressure of 1280 kPa. An *in situ* Mössbauer cell was constructed from stainless steel with 5-mil Kapton (Du Pont Co.) windows. The cell could be evacuated to 10^{-4} Pa and heated by two external heaters. Temperature was measured by two thermocouples within the cell and located near the absorber. The absorber could be heated to 723 ± 7 K. Using this cell, samples were reduced in 101 kPa of flowing hydrogen at a desired temperature and cooled to room temperature in flowing hydrogen. The hydrogen inlet and outlet valves were then closed and the Mössbauer spectrum was recorded at room temperature. For oxidation experiments, previously reduced clays were slowly equilibrated to air during a period of 12 h using a calibrated leak. More severe oxidation treatments were conducted in 101 kPa of flowing oxygen at 473 K for 2 h. These spectra were recorded in oxygen after the cell had been cooled to room temperature.

XRD

Pillared clays were reduced in a Pyrex tube with flowing hydrogen at 673 K for 2 h. Samples were then cooled to room temperature and slowly passivated to air over a 12-h period. Basal spacings were obtained following various reduction and calcining conditions using a Diablo X-ray diffractometer. Copper K_α radiation was used with the samples being scanned from 2.0° to 35.0° at a scanning rate of 1° per minute.

CAEM

The nucleation and growth behavior of pillared clays during reduction was monitored using a specially constructed controlled atmosphere electron microscope employing a JEOL 200CX TEM-STEM equipped with a Gatan 627/628 differentially pumped environmental cell and heating probe. Details involving this technique and apparatus are described elsewhere (*13*).

Clay specimens used during CAEM studies were prepared by finely grinding the clay in a mortar and pestle, dispersing this powder in dry methanol, placing a drop of this suspension onto a holey carbon grid, and allowing the methanol in this suspension to evaporate. Micrographs were generally taken from those portions of a clay particle located directly over a hole in the carbon substrate.

TEM

Transmission electron microscopy studies were performed in a static fashion using a Philips EM-300 electron microscope operated at 60 kV. Pillared clays were pretreated in a manner similar to that of samples prepared for XRD studies. TEM specimens were prepared in a fashion similar to that for CAEM studies except all reduction and passivation treatments had to be performed prior to placing the clay on the holey carbon film.

RESULTS

Mössbauer Studies

100 Al-PILC. The Mössbauer spectrum obtained from the 100 Al-PILC specimen in hydrogen at 298 K is shown in Fig. 1a. The

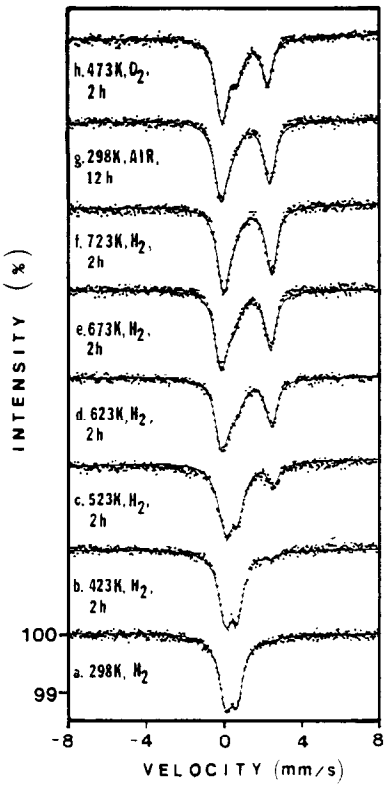

FIG. 1. Room temperature Mössbauer spectra of 100 Al-PILC after various reduction/oxidation treatments under the conditions indicated.

spectrum consists of a broadened Fe^{3+} doublet with a peak width (FWHM) of 0.74 mm/s at an isomer shift of 0.35 mm/s along with a small Fe^{2+} doublet centered at 0.93 mm/s. The fitted Mössbauer parameters including isomer shift (I.S.), quadrupole splitting (Q.S.), and hyperfine splitting (H.F.), as listed in Table 1, are in agreement with those obtained from montmorillonite by Rozenson and Heller-Kallai (*14*) and Cardile and Johnston (*15*). The Mössbauer features observed in Fig. 1 are caused by the substitution of iron impurities into the Al^{3+} octahedral sites of montmorillonite. This iron content, which can be as high as 2.5 wt%, composes the background iron component present in montmorillonite. The reduction characteristics of these structural iron impurities have been studied so that the spectral features corresponding to these impurities can be discounted from subsequent spectra recorded from samples containing intentionally intercalated iron.

The broadness of the Fe^{3+} resonance in Fig. 1 has been attributed to a distribution of octahedral sites having different environments (e.g., *trans* and *cis* arrangements of OH^- ions) (*14*). However, the question of which of these octahedral sites is occupied by iron is controversial (*15*). The relatively small Fe^{3+} quadrupole splitting (ca. 0.58 mm/s) and large Fe^{2+}quadrupole splitting (ca. 2.65 mm/s) obtained from 100 Al-PILC suggests that iron sites in montmorillonite are highly symmetric in nature (e.g., octahedral sites). Both the Fe^{3+} and the Fe^{2+} quadrupole splittings decrease with increasing reduction temperature (see Table 1) suggesting that Fe^{3+} at less symmetric sites may preferentially reduce to Fe^{2+} allowing the Fe^{3+}, which persists at more symmetric sites, to lower the average quadrupole splitting recorded for the remaining Fe^{3+}.

As shown in Fig. 1f, structural iron could not be reduced to the metallic state following reduction up to 723 K; however, 78.8% of the total spectral area was reduced to Fe^{2+}. Similar reduction behavior for structural iron was observed by Rozenson and Heller-Kallai (*16*). They showed that ca. 80% of the structural iron in montmorillonite could be reduced to Fe^{2+} following treatment with hydrazine vapor at 343 K. A reduction mechanism involving hydrogen atom penetration from the interlamellar space to the octahedral sites was proposed. On the basis of this mechanism, the observed reduction of structural iron to Fe^{2+} in 100 Al-PILC may be explained by the penetration of hydrogen atoms into the clay layers, although, the clay, by itself, is not expected to be a good dissociator of molecular hydrogen.

Exposing the sample slowly to air over a period of 12 h following reduction at 723 K (see Fig. 1g) caused less than a 5% conversion of Fe^{2+} to Fe^{3+}. Also, following oxidation at 473 K for 2 h in 101 kPa of flowing

TABLE 1

Fitted Parameters of Mössbauer Spectra Shown in Figs. 1 through 5

Spectrum/ figure	Fe^{3+}			Fe^{2+}			Fe^{0}	
	I.S.	Q.S.	% Area	I.S.	Q.S.	% Area	H.F.	% Area
1a	0.35	0.58	98.5	0.93	2.63	1.5	—	—
1b	0.36	0.57	93.0	1.28	2.64	7.0	—	—
1c	0.35	0.56	70.9	1.18	2.64	29.1	—	—
1d	0.34	0.54	40.7	1.14	2.63	59.3	—	—
1e	0.31	0.47	32.0	1.20	2.60	68.0	—	—
1f	0.26	0.40	21.2	1.11	2.52	78.8	—	—
1g	0.28	0.44	24.4	1.12	2.53	75.6	—	—
1h	0.35	0.71	48.6	1.09	2.40	51.4	—	—
2a	0.37	0.76	100.0	—	—	—	—	—
2b	0.36	0.79	100.0	—	—	—	—	—
2c	0.39	0.79	97.4	0.90	2.47	2.6	—	—
2d	0.39	0.79	78.9	1.07	2.27	8.1	317	13.0
2e	0.39	0.81	73.5	1.14	2.37	11.0	316	15.5
2f	0.40	0.83	56.8	1.18	2.21	15.2	319	28.0
2g	0.40	0.78	64.2	1.04	2.40	15.7	314	20.1
2h	0.37	0.88	96.0	1.16	2.46	4.0	—	—
2i[a]	0.38	0.70	87.5	1.11	2.54	12.5	—	—
2j[a]	0.40	0.77	76.5	1.01	2.31	23.5	—	—
2k[a]	0.39	0.85	38.8	1.06	2.08	27.8	313	33.4
2l[a]	0.35	0.67	14.4	1.09	2.51	22.8	314	62.8
2m[a]	0.37	0.68	35.4	1.02	2.57	7.6	317	27.8
2n[a]	0.37	0.85	91.8	1.01	0.70	8.2	—	—
3a	0.37	0.77	100.0	—	—	—	—	—
3b	0.38	0.81	97.6	0.95	2.46	2.4	—	—
3c	0.39	0.71	28.3	1.12	2.34	26.3	308	45.4
3d	0.38	0.79	89.5	1.10	2.46	10.5	—	—
3e	0.38	0.71	29.8	1.03	2.36	25.8	304	44.4
3f	0.39	0.70	84.9	0.97	2.34	15.1	—	—
3g	0.38	0.78	30.3	1.02	2.24	26.5	305	43.2
4a	0.37	0.69	100.0	—	—	—	—	—
4b	0.36	0.79	100.0	—	—	—	—	—
4c	0.36	0.84	100.0	—	—	—	—	—
4d	0.37	0.86	85.2	1.12	2.59	14.8	—	—
4e	0.39	0.87	82.4	1.17	2.57	17.6	—	—
4f	0.38	0.85	85.5	1.07	2.52	17.5	—	—
4g[a]	0.37	0.73	100.0	—	—	—	—	—
4h[a]	0.33	0.73	19.6	1.13	2.30	80.4	—	—
4i[a]	0.38	0.74	12.4	1.10	2.19	87.6	—	—
4j[a]	0.34	0.69	9.0	1.10	2.22	90.1	—	—
4k[a]	0.36	0.75	9.5	1.12	2.29	80.5	317	10.3
4l[a]	0.38	0.84	100.0	—	—	—	—	—
5a	0.34	0.74	100.0	—	—	—	—	—
5b	0.32	0.75	100.0	—	—	—	—	—
5c	0.39	0.71	74.0	1.01	2.29	26.0	—	—
5d	0.39	0.51	42.9	1.11	2.11	57.1	—	—
5e	0.39	0.45	22.7	1.11	2.07	77.3	—	—
5f	0.35	0.97	94.8	0.97	2.52	5.2	—	—

TABLE 1—*Continued*

Spectrum/ figure	Fe^{3+}			Fe^{2+}			Fe^{0}	
	I.S.	Q.S.	% Area	I.S.	Q.S.	% Area	H.F.	% Area
5g[a]	0.37	0.71	100.0	—	—	—	—	—
5h[a]	0.38	0.64	55.1	0.86	2.45	44.9	—	—
5i[a]	0.33	0.47	44.2	1.07	2.06	55.8	—	—
5j[a]	0.35	0.64	43.7	0.84[b]	1.31	22.5	—	—
				1.01[c]	2.00	33.8		
5k[a]	0.37	0.58	47.2	0.88[b]	1.24	21.6	—	—
				1.02[c]	2.20	31.2		
5l[a]	0.36	0.68	67.3	1.04	2.50	22.7	—	—

Note. Known contributions of structural iron in specimens 2a through 5l have *not* been included in this table but are retained in the spectra of Figs. 1–5. Details concerning reduction/oxidation treatments applied to these specimens are denoted in the appropriate figures/spectra as well as the description of experimental procedures. Spectra 1a–1h are from 100 Al-PILC; Spectra 2a–2n are from 100 Fe-PILC; Spectra 3a–3h are from 75/25 Fe/Al-PILC; Spectra 4a–4l are from 50/50 Fe/Al-PILC; Spectra 5a–5l are from alloy-PILC. I.S., isomer shift (mm/s) with reference to metallic iron. Q.S., quadrupole splitting (mm/s). H.F., hyperfine field (kOe).

[a] Approximately 1 wt% Pt has been added to these specimens.

[b] Tetrahedral Fe^{2+} sites.

[c] Octahedral Fe^{2+} sites.

oxygen, 51.4% of the spectral area still remained as Fe^{2+} (see Fig. 1h). These results provide additional evidence that after reduction structural iron did not lie on the surface of the clay layers. The quadrupole splitting of Fe^{3+} increased from 0.58 to 0.71 mm/s while the quadrupole splitting of Fe^{2+} decreased from 2.63 to 2.40 mm/s following the reduction/oxidation steps, indicating that these treatments caused some distortion of the octahedral sites.

100 Fe-PILC. Mössbauer spectra obtained from 100 Fe-PILC following various reduction and oxidation treatments are shown in Fig. 2. It should be noted that all the spectra shown for this sample, as well as the other samples containing pillared iron in this study, contain contributions from both structural and intercalated iron. Because of the favorable enrichment of intercalated iron in ^{57}Fe, spectral areas corresponding to structural iron are always 10% or less of the total spectra area depending on the amount and enrichment of the intercalated iron used. It should be noted that the data shown in Table 1 are presented after removing the expected contributions provided by structural iron. This subtraction procedure has been accomplished by fitting the spectra obtained from iron-intercalated specimens with additional Fe^{2+} and Fe^{3+} doublets constrained to have the same spectral parameters as those obtained from 100 Al-PILC specimens following equivalent chemical treatments. The weight of individual sample pellets has also been scaled so that each specimen contains an equivalent amount of structural iron.

While it is possible that the presence of intercalated iron can affect the reduction characteristics of structural iron through a favorable interaction with molecular hydrogen, in the absence of a better understanding of this potentially synergistic interaction, a simple subtraction procedure has been utilized to obtain the data listed in Table 1. Fe^{3+} and Fe^{2+} resonances provided by intercalated iron were also fit with symmetric doublets. A narrow Fe^{3+} doublet with a peak width of 0.44 mm/s, compared to that of 100 Al-PILC (ca. 0.74 mm/s), was observed in the spectrum obtained at 298 K in hydrogen (see Fig. 2a). The Fe^{3+} quadrupole splitting was much larger than that of

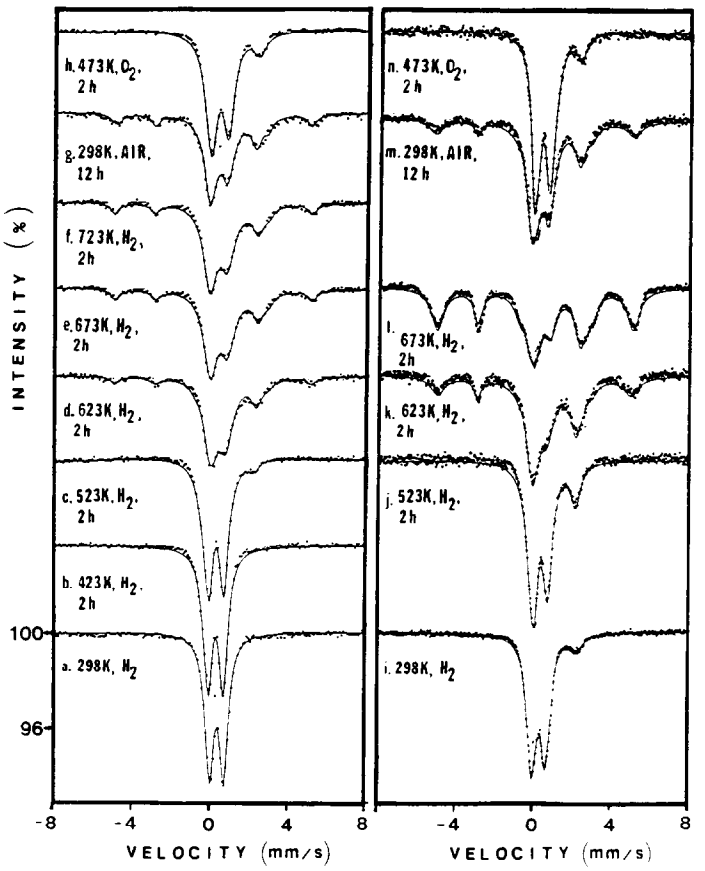

FIG. 2. Room temperature Mössbauer spectra of 100 Fe-PILC (Spectra a through h) and 100 Fe-PILC impregnated with 0.98 wt% Pt (Spectra i through n) after various reduction/oxidation treatments under the conditions indicated.

100 Al-PILC (0.76 versus 0.58 mm/s) suggesting that iron sites located in the interlayer region are less symmetric (i.e., more distorted (*17*) than those located within the montmorillonite structure.

The spectrum shown in Fig. 2c obtained following reduction at 523 K shows some reduction (ca. 2.6% spectral area) to Fe^{2+} as indicated by a distinct shoulder at 2.21 mm/s. This component grows in intensity following reduction at higher temperatures, as does the distinct sextuplet of metallic iron (see Figs. 2d–2f, and Table 1). Following reduction at 723 K, 28.0 and 15.2% of the total spectral area belong to metallic iron and Fe^{2+}, respectively. As seen from Table 1, the Fe^{3+} quadrupole splitting increases with increasing reduction temperature while the Fe^{2+} quadrupole splitting decreases. These trends suggest that either pillared iron sites become more distorted prior to formation of metallic iron or more symmetric Fe^{2+} and Fe^{3+} sites are preferentially reduced leaving the distorted sites behind. It should be noted that this trend for the quadrupole splitting of Fe^{3+} is opposite that observed for the reduction of structural iron (i.e., 100 Al-PILC).

The hyperfine field of the metallic iron sextuplet is reduced substantially (ca. 317 kOe) compared to the expected bulk value of 330 kOe at 298 K. Furthermore, the widths of the outermost peaks of the sextuplet increase from 0.42 mm/s, obtained

from an iron foil calibration standard, to 0.86 mm/s for the reduced clay. The reduced hyperfine field and the broadened peaks suggest formation of small iron particles exhibiting magnetic relaxation. In the collective magnetic excitation model proposed by Mørup *et al.* (*18, 19*), small thermal excitations of the magnetization vector around a low-energy direction of magnetically ordered microcrystals cause a substantial decrease in the hyperfine field. Broadening of Mössbauer lines is also observed from small particles as a result of crystallite size distributions and distributions of hyperfine fields caused by surface and/or impurity effects (*20–24*).

It is generally recognized that shape anisotropy provides a dominant contribution to the magnetoanisotropy energy constant, K, for small iron particles (*19*). Thus, using shape anisotropy values of 5×10^4 and 8.5×10^5 J/m^3 (viz., corresponding to prolate crystallites with major to minor axis ratios of 2 and 10, respectively) it is possible to calculate crystallite volumes of (4.7 nm)^3 and (3.9 nm)^3 in conjunction with the observed hyperfine field of 317 kOe (*18, 19*). Although the theory of collective magnetic excitation is useful for estimating the average particle size in this manner, the uncertainty associated with choosing the correct value for K limits its utility unless crystallite shapes and sizes can be determined by additional means (*19*). A superparamagnetic singlet, corresponding to metallic iron particles less than ca. (3.0 nm)^3 (*25–27*), was not visible in the spectra shown in Fig. 2, although only room temperature spectra were recorded.

In order to ascertain whether metallic iron particles were accessible to the gas phase or encapsulated within a collapsed clay structure, the previously reduced clay was slowly exposed and allowed to equilibrate in 21 kPa of oxygen (i.e., air) for 12 h (Figs. 2g and 2h). Following this exposure, the metallic iron content decreased from 28.0 to 20.1% of the total spectral area while the spectral area associated with Fe^{3+} increased by 7.4%, suggesting that metallic iron was converted to Fe^{3+}. The decrease in metallic iron was accompanied by a decrease in the hyperfine field to ca. 314 kOe indicating that metallic iron domains became smaller after passivation possibly due to the formation of an iron oxide skin on the metal. More severe oxidation at 473 K in 101 kPa of oxygen eliminated all traces of metallic iron and most all of the Fe^{2+} (see Table 1).

As can be seen from Figs. 2i through 2n, the effect of platinum on the reduction behavior of 100 Fe-PILC was substantial. A total of 12.5% of the spectral area are reduced to Fe^{2+} at 298 K in hydrogen (Fig. 2i). The corresponding percentage of metallic iron increased from 15.5% without platinum (Fig. 2e) to 62.8% with platinum (Fig. 2l) following reduction at 673 K. Despite differences in the degree of reduction to metallic iron, the Pt-impregnated sample provided similar trends in the Fe^{3+} and Fe^{2+} quadrupole splittings and the value of the hyperfine field. Oxidation behavior also appeared similar regardless of whether or not platinum had been added to the specimen. Mössbauer features attributable to the formation of small Fe–Pt alloy particles were not observed from any of the samples containing platinum (*28, 29*) suggesting that increased reducibility of iron was accomplished via hydrogen spillover from discrete platinum crystallites.

75/25 Fe/Al-PILC. As seen from Fig. 3 and Table 1, 75/25 Fe/Al-PILC provided reduction behavior and Mössbauer parameters similar to those observed from 100 Fe-PILC. However, several differences were noted. First, the spectral area belonging to metallic iron following reduction at 673 K increased from 15.5% (Fig. 2e) to 45.5% (Fig. 3c). Second, the oxidation behavior was different such that all of the metallic component could be oxidized back to Fe^{3+} following treatment in 21 kPa of oxygen at 298 K (Fig. 3d). Third, the hyperfine field of this sample (ca. 308 kOe) was smaller than that of 100Fe-PILC.

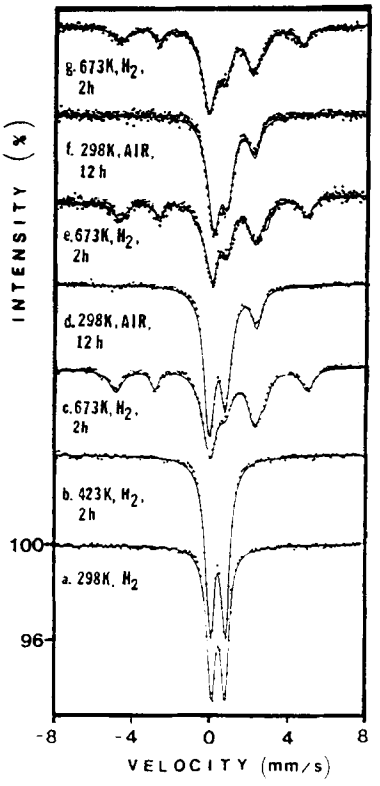

FIG. 3. Room temperature Mössbauer spectra of 75/25 Fe/Al-PILC after various reduction/oxidation treatments under the conditions indicated.

In order to check the stability of the reduced iron phase, additional reduction and oxidation treatments were performed on the specimen shown in Fig. 3d. The spectrum shown in Fig. 3e, for example, was obtained after completing the following treatment sequence: (i) re-reduction at 673 K in flowing hydrogen for 2 h, (ii) exposure to air for 12 h, and (iii) an additional reduction treatment at 673 K for 2 h. Spectra shown in Figs. 3f and 3g were obtained after repeating steps (ii) and (iii), respectively. The reproducibilities of the Mössbauer parameters following each cycle are shown in Table 1. These data indicate that reduced iron particles can be reformed to their initial states and presumably their initial dimensions in the absence of extensive sintering or encapsulation.

50/50 Fe/Al-PILC. Following reduction at temperatures below 673 K, this specimen provided Fe^{2+} and Fe^{3+} Mössbauer trends similar to those observed from 100 Fe-PILC and 75/25 Fe/Al-PILC. However, 50/50 Fe/Al-PILC could not be reduced to metallic iron at temperature of 673 K or higher as shown in Fig. 4. Initially, the reduction process was suspected of being diffusion-limited and less spontaneous as a result of the increased number of aluminum pillars located between the iron pillars in the interlayer region. In order to test this hypothesis, the sample was reduced for an extended period of time (i.e., 12 h, 673 K, 101 kPa of hydrogen). The spectrum obtained following this reduction treatment (Fig. 4f) was nearly identical to that obtained following reduction for 2 h (Fig. 4e). Comparison of the various specimens shown in Table 1 indicated that 50/50 Fe/Al-PILC was the most difficult sample to reduce to the metallic state. Moreover, reduction at 523 K did not produce any Fe^{2+}, whereas 100 Fe-PILC and 75/25 Fe/Al-PILC specimens showed significant reduction to Fe^{2+} under these conditions.

In the presence of platinum, a vast majority of iron atoms (ca. 80.4%) were reduced to Fe^{2+} following reduction at 423 K (Fig. 4h). It should also be noted that the amount of Fe^{3+} reduced to Fe^{2+} for platinum-containing 50/50 Fe/Al-PILC specimens was greater than that obtained from the platinum-containing 100 Fe-PILC sample under these same reduction conditions. The spectral area associated with Fe^{2+} steadily increased with reduction temperature, until at 673 K, 10.3% of the spectral area resulted from metallic iron (Fig. 4k). The hyperfine field associated with the metallic iron was ca. 317 kOe. Following passivation in air, the metallic iron and Fe^{2+} components were oxidized almost completely to Fe^{3+}, as shown in Fig. 4l.

Alloy-PILC. This sample could not be reduced to metallic iron in the presence or absence of platinum following reduction to 673 K (Fig. 5). The Fe^{2+} and Fe^{3+} isomer shifts and quadrupole splittings obtained

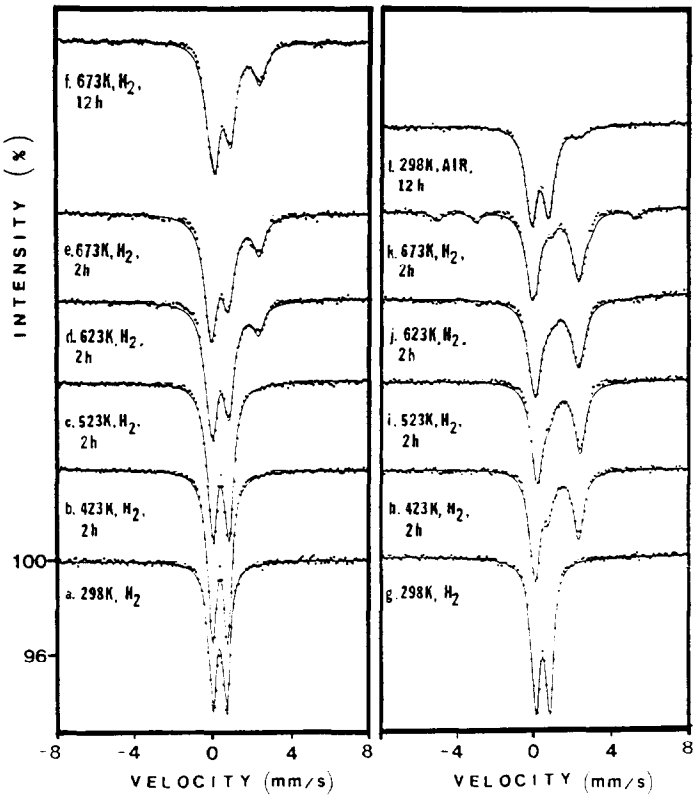

FIG. 4. Room temperature Mössbauer spectra of 50/50 Fe/Al-PILC (Spectra a through f) and 50/50 Fe/Al-PILC impregnated with 1.08 wt% Pt (Spectra g through l) after various reduction/oxidation treatments under the conditions indicated.

from this sample were in the range of those determined from 100 Al-PILC. Both the Fe^{3+} and Fe^{2+} quadrupole splittings decreased with increasing reduction temperature. These trends may indicate that lower coordination iron atoms located near the pillar–gas interface were progressively reduced to Fe^{2+} while the remaining Fe^{3+} atoms occupied increasingly more symmetric and difficult to reduce sites within the interior of the structure. A small amount of Fe^{2+} (ca. 5.2%) was still observed following oxidation at 473 K (Fig. 5f) indicating that some Fe^{2+} was located within the pillars or encapsulated by clay layers.

In the presence of platinum, formation of a spinel-like structure was suspected based on the appearance of a small shoulder at 1.46 mm/s following reduction at 673 K (Fig. 5j). The spectrum was fitted with three symmetric doublets corresponding to octahedral Fe^{3+}, tetrahedral Fe^{2+}, and octahedral Fe^{2+}. The fitted parameters agreed well with those obtained from $FeAl_2O_4$ (*30, 31*). Exposing the reduced sample slowly to air did not remove the shoulder at 1.46 mm/s (Fig. 5k) suggesting that tetrahedral sites were located within the alloy pillars. The intensity of the tetrahedral Fe^{2+} peak could be reduced following oxidation in 101 kPa of oxygen at 473 K (Fig. 5l). After such treatments, 22.7% of the spectral area still belonged to the octahedral Fe^{2+} doublet. These results indicate that platinum facilitates the degree of mixing/reaction between iron atoms and the aluminum oxide host. Therefore, it was suspected that tetrahedral Fe^{2+} sites (i.e., spinel-like sites) were cre-

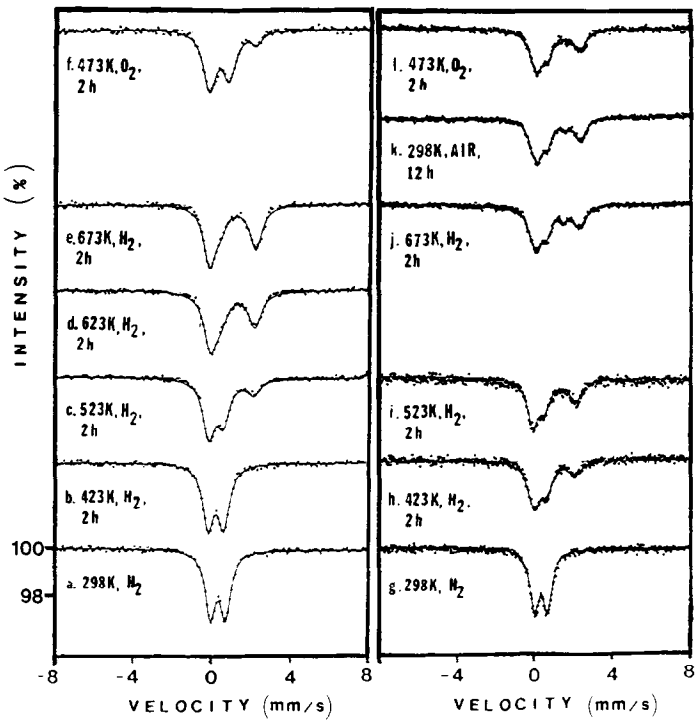

FIG. 5. Room temperature Mössbauer spectra of alloy-PILC (Spectra a through f) and alloy-PILC impregnated with 1.04 wt% Pt (Spectra g through l) after various reduction/oxidation treatments under the conditions indicated.

ated inside of the alumina matrix from a solid–solution of iron cations and the alumina host.

The reduction behavior of this sample is similar to the behavior of supported iron catalysts of low loading on alumina where reduction below Fe^{2+} is difficult (*32–34*) and spinel-like structures are obtained (*33, 34*). It is generally recognized that the interaction between iron and alumina at low iron loadings is too strong to allow formation of metallic iron.

XRD and BET Studies

The stability of the pillared clays was also examined using XRD and BET techniques. The X-ray basal spacings, d_{001}, of clay samples following various treatments are shown in Table 2, while the N_2 BET surface areas of these specimens are plotted versus reduction temperature in Fig. 6. The *d*-spacings and BET surface areas for a given sample appear to correlate with one another with higher *d*-spacings conforming to more open structures possessing higher surface areas.

Clays intercalated with discrete aluminum pillars such as 100 Al-PILC, 50/50 Fe/

TABLE 2

X-Ray Basal Spacings, d_{001} (nm), of Pillared Clays after Various Treatments

Samples	As prepared	Calcined at 673 K[a]	Reduced at 673 K[b]	Reduced at 673 K w/Pt[c]
100 Al-PILC	1.86	1.67	1.73	1.73
50/50 Fe/Al-PILC	1.90	1.61	1.61	1.67, 1.36
75/25 Fe/Al-PILC	1.84	1.48	1.70	1.47
Alloy-PILC	1.56	1.37	1.32	1.28
100 Fe-PILC	1.38	1.07	0.98	0.98
Na-montmorillonite	1.19	—	0.99	—

[a] Calcined in air for 45 min.
[b] Reduced in 101 kPa of flowing hydrogen for 2 h.
[c] Impregnated with ca. 1.0 wt% platinum and reduced in 101 kPa of flowing hydrogen for 2 h.

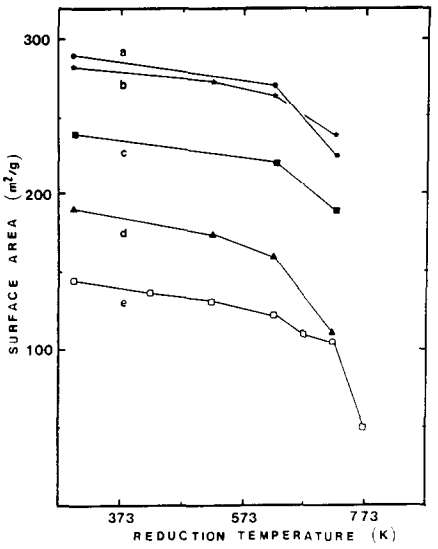

FIG. 6. BET surface areas of pillared clays as a function of reduction temperature: (a) 100 Al-PILC, (b) 50/50 Fe/Al-PILC, (c) 75/25 Fe/Al-PILC, (d) alloy-PILC, and (e) 100 Fe-PILC. All samples were reduced in a sequential fashion in 101 kPa of flowing hydrogen for 2 h at the temperature indicated prior to BET measurements.

Al-PILC, and 75/25 Fe/Al-PILC have higher surface areas ($\geq$240 m^2/g) and larger *d*-spacings ($\geq$1.84 nm) than 100 Fe-PILC and alloy-PILC materials. These values suggest that discrete aluminum pillars are in fact derived from $Al_{13}O_4(OH)_{24}^{7+}$ species (*3*, *35*). The smaller surface area of 75/25 Fe/Al-PILC is likely due to the decreased number of aluminum pillars.

The surface area of 100 Fe-PILC (ca. 144 m^2/g) was the lowest among all samples examined. A *d*-spacing of 1.38 nm, corresponding to an interlayer spacing of ca. 0.4 nm, appears to be too small to allow the existence of numerous "polynuclearic" $Fe_3(OH)_4^{3+}$ pillars since it has been reported that montmorillonite, pillared with "polynuclearic" $Fe_3(OH)_4^{3+}$ species, has BET surface areas greater than 300 m^3/g and *d*-spacings of ca. 2.0 nm (*17*). For this reason, it is suspected that iron pillars found in 100 Fe-PILC and the mixed pillared systems (i.e., 75/25 Fe/Al-PILC and 50/50 Fe/Al-PILC) are likely derived from primarily "mononuclearic" $Fe_3(OH)_4^{5+}$ cations.

Alloy-PILC had a surface area and *d*-spacing of 180 m^2/g and 1.56 nm, respectively. These values suggest that alloy pillars are smaller in size than $Al_{13}O_4(OH)_{24}^{7+}$ pillars, but larger than $Fe_3(OH)_4^{5+}$ pillars. As can be seen from Fig. 6, the surface areas of these samples decreased significantly following reduction at 673 K, suggesting some instability.

The 100 Al-PILC, 50/50 Fe/Al-PILC, and 75/25 Fe/Al PILC samples retained their expanded structures following reduction to 723 K. The low *d*-spacing of 100 Fe-PILC (ca. 0.98 nm) indicated that this structure collapsed following reduction at 673 K, while BET measurements suggested that significant surface area (ca. 105 m^2/g) was still present.

The effect of platinum on *d*-spacing was evident only in samples containing mixed-metal pillars. For 75/25 Fe/Al-PILC, the *d*-spacing decreased from 1.70 nm, in the absence of platinum, to 1.47 nm, in the presence of platinum, following reduction at 673 K. The 50/50 Fe/Al-PILC inpregnated with 0.97 wt% Pt provided two XRD peaks following reduction at 673 K: a sharp peak, corresponding to expanded clay layers with *d*-spacing of 1.67 nm, and a broad peak, corresponding to distorted clay layers with *d*-spacings of 1.36 nm.

TEM AND CAEM Studies

Results obtained from CAEM and TEM studies are qualitatively summarized in Table 3. Nucleation and crystallite growth during and after reduction have been classified into four categories depending on the density, size, and general observability of point sources of high contrast (i.e., crystallites). These categories of nucleation and growth have been defined as "none" < "minor" < "uniform" < "massive." Verification that regions of high contrast were crystalline in nature was provided by dark-field imaging techniques. An exemplary transmission electron micrograph of a sam-

TABLE 3

Summary of Results Obtained from TEM and CAEM Studies

Sample	Temp. (K)	TEM	CAEM
100	673	None	None
Al-PILC	823	—	None
Alloy-PILC	673	None	None
	823	—	None
100	673	Massive	None
Fe-PILC	823	—	Massive
75/25	673	Uniform	—
Fe/Al-PILC	823	—	—
50/50	673	Minor	None
Fe/Al-PILC	823	—	Uniform

Note. The severity and general observance of nucleation and growth of high-contrast domains (i.e., crystallites) is denoted in the order None < Minor < Uniform < Massive. TEM reduction conditions: 101 kPa, H_2, 2h, at temperature indicated. CAEM reduction conditions: 133 Pa, H_2. Specimen held at 473 K for ca. 1 h → temperature increased to 673 K and held constant for 25 min (observation made above) → temperature increased to 823 K and held constant for 25 min (observation made above).

ple providing observable nucleation and growth (i.e., 75/25 Fe/Al-PILC) is shown in Fig. 7. Electron micrographs, corresponding to *in situ* images recorded via CAEM were also collected and an exemplary sequence obtained from 100 Fe-PILC is shown in Fig. 8.

TEM indicates that iron pillars nucleate and grow into crystallites following reduction at 673 K, as evidenced by the appearance of numerous high-contrast features of ca. 10 to 40 nm in diameter. More pronounced nucleation and growth were observed from samples containing higher iron loadings, suggesting that these features are associated with iron-containing materials.

CAEM reduction behavior did not precisely mimic the nucleation and growth behavior observed by TEM. This discrepancy has been attributed to the lower hydrogen pressures and shorter reduction times used prior to recording the CAEM images (i.e., CAEM, 133 Pa of H_2 for 25 min; TEM, 101 kPa of H_2 for 2 h). Despite the "sluggishness" associated with reduction in the CAEM, this technique did allow observation of the same field of view during the entire course of the reduction process. Since the behavior observed is qualitatively similar to that observed using TEM, it is possible to conclude that the trends observed via TEM are valid indicators of morphology throughout the specimen and not artifacts of the heterogeneous nature of the clays.

According to the Mössbauer results discussed earlier, reduced 75/25 Fe/Al-PILC specimens contained no metallic iron following passivation in air and 50/50 Fe/Al-PILC specimens did not provide any metallic iron following reduction. Therefore, the appearance of large crystallites in the TEM micrographs of reduced and passivated 75/25 Fe/Al-PILC and 50/50 Fe/Al-PILC cannot be associated with metallic iron. Additional micrographs taken of clay particles removed from Mössbauer pellets following reduction and passivation revealed that significant differences in specimen morphology were not caused by temperature gradients across the Mössbauer pellet or other differences in the various reduction cells. Thus, comparison of Mössbauer and electron microscopic data indicates that the large nucleated features observed in Figs. 7 and 8 must stem primarily from the migration and coalescence of iron oxide pillars into iron oxide crystallites.

In comparing the data obtained from Mössbauer spectroscopy and electron microscopy, it is important to note that iron oxide particles of α-Fe_2O_3 which are $\leq$15 nm in diameter will appear as Fe^{3+} doublets in the room temperature Mössbauer spectrum due to magnetic relaxation (*36*). Alternatively, metallic iron crystallites of ca. 3–4 nm in diameter, which were detected by means of Mössbauer spectroscopy in reduced and passivated 100 Fe-PILC, may be too thin and/or too small to be detected by TEM or CAEM because of difficulties involving contrast differentiation with the clay. The distinctly observable nature of

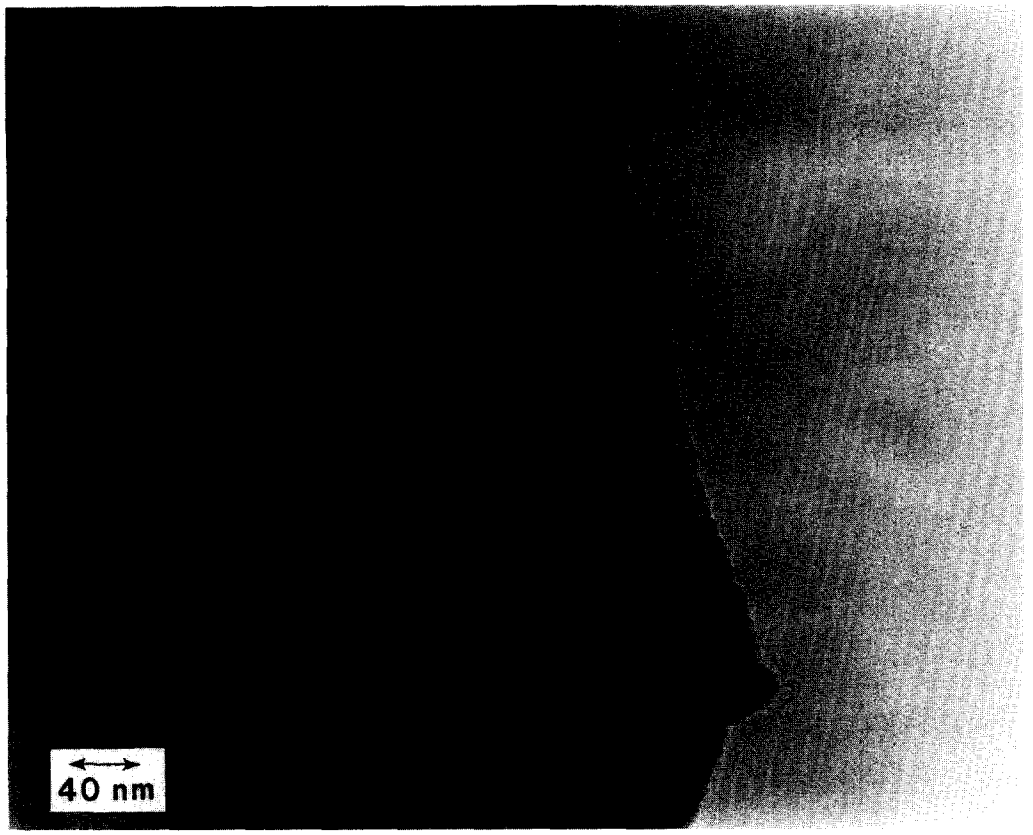

FIG. 7. Electron micrograph (TEM) of 75/25 Fe/Al-PILC reduced in 101 kPa of hydrogen for 2 h at 673 K.

the iron oxide crystallites indicates that these structures must possess three-dimensional character. Reduction mechanisms leading to the formation of these particles, their location and accessibility within the clay, and the effects of these particles on the overall stability of the layered structure are discussed below.

DISCUSSION

Size and Integrity of Pillars in Mixed Pillared Systems

XRD and BET results demonstrate that the expanded structures of mixed pillared clays (e.g., 75/25 Fe/Al-PILC and 50/50 Fe/Al-PILC) are similar to those of 100 Al-PILC (viz., high *d*-spacing and surface area). The smaller *d*-spacing and surface area of 100 Fe-PILC indicate that iron pillars are smaller than aluminum pillars. The interlayer spacings of pillared clays containing discrete aluminum pillars are ca. 0.9 nm compared to ca. 0.4 nm for 100 Fe-PILC. Thus, for mixed pillared systems the contributions from iron pillars to separate and hold the clay layers apart is suspected to be small. The expanded structure of the mixed pillared clays appears to be stabilized by the largest of the pillars, namely the aluminum pillars, as shown in Fig. 9A.

The above argument answers one of the objectives of the present investigation, that mixed pillared clays do not appear to be intercalated with species which contain iron and aluminum in the same complex, but rather with discrete aluminum pillars and discrete iron pillars. This is further sup-

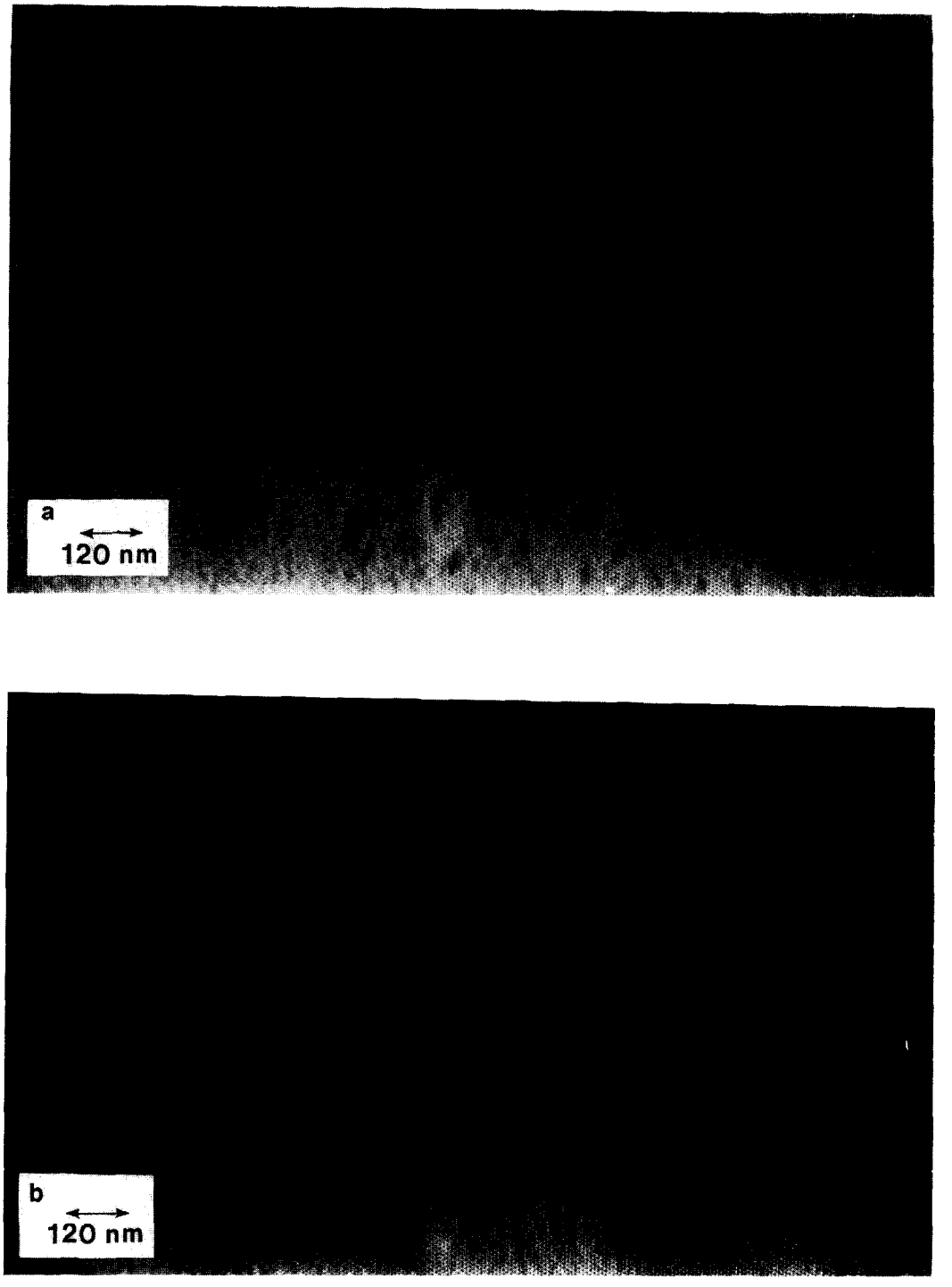

FIG. 8. Electron micrographs (CAEM) of 100 Fe-PILC specimen in 133 Pa H_2; (a) as prepared on holey carbon film after 1 h at 473 K; (b) same field of view as (a) following 25 min at 673 K and an additional 25 min at 823 K.

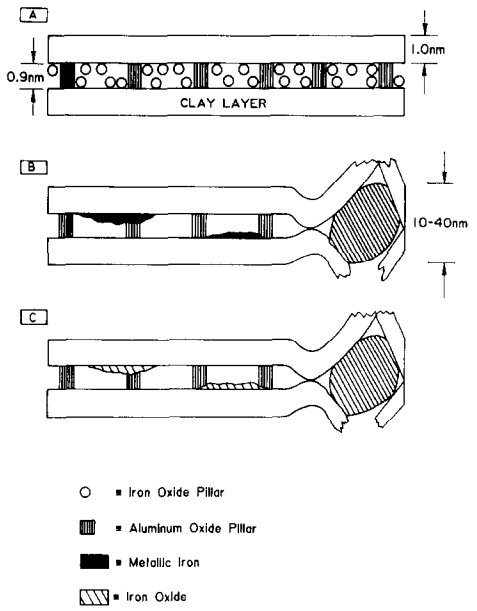

FIG. 9. Schematic representation of 75/25 Fe/Al-PILC: (A) as prepared after freeze-drying, (B) after reduction in 101 kPa of hydrogen for 2 h at 673–723 K, and (C) after slow passivation for 12 h in 21 kPa of oxygen at 298 K.

ported by the fact that the properties of alloy-PILC during reduction are different from those obtained from mixed pillared clays containing discrete iron and aluminum species.

XRD and BET results indicate that mixed pillared clays are relatively stable after reduction to 673–723 K. Decreases in the *d*-spacing and surface area are relatively small compared to 100 Fe-PILC, suggesting that the stability of mixed pillared clays arises from the irreducible nature of aluminum oxide pillars under these conditions.

TEM and CAEM studies show that large iron oxide particles (ca. 10 to 40 nm) are formed following reduction at 673 K. It is expected that some clay layers must be destroyed and/or collapse as a result of the formation of these large particles. However, since mixed pillared clays still possess BET surface areas greater than ca. 200 m^2/g after reduction at 723 K, it appears that nucleation and growth of iron oxide domains do little to affect the stability of the surrounding structure (Fig. 9B).

Synthesis, Accessibility, and Stability of Metallic Iron Domains

Formation. Reduced hyperfine fields and broadened lines observed in the Mössbauer spectra of 100 Fe-PILC and 75/25 Fe/Al-PILC indicate the formation of small metallic iron domains, which may be in the form of three-dimensional crystallites and/or thin-film/pancake-type islands of somewhat larger lateral extent. Using the theory of collective magnetic excitations (*18, 19*) and a hyperfine field of 304 kOe (Fig. 3f), it is possible to bracket the minimum volume of these domains somewhere in the $(3.1–4\ nm)^3$ range pending application of appropriate assumptions. Comparison of these Mössbauer results with TEM observations indicates that large iron oxide particles are formed within these clays at the same time. On the basis of these results, and the structural information provided by XRD and BET surface area measurements, a schematic representation for the reduction process of 100 Fe-PILC is shown in Figs. 10A and 10B. Relatively small mononuclearic $Fe_3(OH)_4^{5+}$ pillars, as evidenced by the small *d*-spacings (ca. 1.38 nm) and low surface areas (ca. 144 m^2/g) obtained from 100 Fe-PILC, are believed to be present following ion exchange and freeze-drying (Fig. 10A). It is from this precursor stage that both small metallic iron domains and somewhat larger iron oxide particles are formed.

During reduction, iron oxide pillars are decomposed via a redox reaction involving dissociated hydrogen and coalesce in the interlayer region to form domains large enough to stabilize metallic iron on/within the clay (Fig. 10B). The layered structure of the clay may force some iron atoms to nucleate and grow in the form of pancake-shaped crystallites; however, because larger metallic domains must form at the expense of the layered structure, this behavior is not as prevalent as with 75/25 Fe/Al-PILC (Fig. 9B).

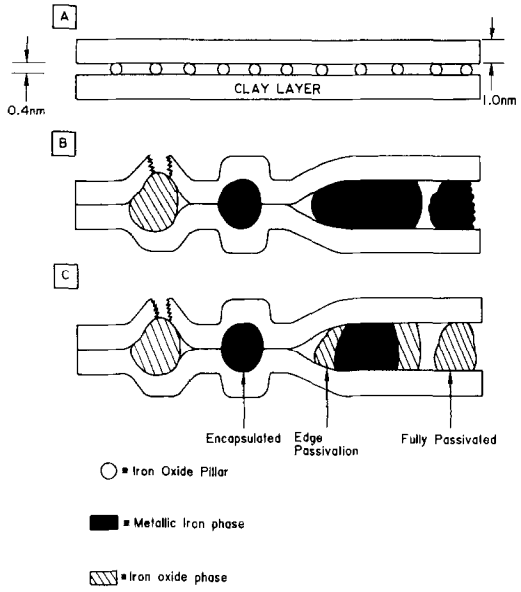

FIG. 10. Schematic representation of 100 Fe-PILC: (A) as prepared after freeze-drying, (B) after reduction in 101 kPa of hydrogen for 2 h at 673–723 K, and (C) after slow passivation for 12 h in 21 kPa of oxygen at 298 K.

The *d*-spacing of the reduced clay (ca. 1.7 nm) and surface area (ca. 200 m^2/g) indicate that the expanded structure of 75/25 Fe/Al-PILC is still relatively intact following reduction up to 673 K as expected from the presence of the more reduction-resistant aluminum pillars (Fig. 9B). This expanded structure is apparently responsible for the formation of greater amounts of metallic iron in 75/25 Fe/Al-PILC (ca. 45.5%) than in 100 Fe-PILC (15.5%), even though 100 Fe-PILC contains significantly more iron (*12*).

Accessibility. During the reduction process, a partial collapse of the 100 Fe-PILC clay structure is observed as indicated by a decrease in the *d*-spacing to 0.98 nm. As a result, reduced iron domains may become partially encapsulated by one of at least two different mechanisms (Fig. 10B). The first mechanism can be thought of as an admixture of iron crystallites which are either totally exposed or completely encapsulated and which passivate in oxygen accordingly (Fig. 10C). Alternatively, a second mechanism/approach is to view the crystallites as more uniform in nature but exposed to the gas phase only around their edges.

Evidence for partial encapsulation of metallic iron domains, by either of the above two mechanisms, is supported by air-passivation experiments. When these procedures are applied to 100 Fe-PILC only a small portion of metallic iron is oxidized to either Fe^{2+} or Fe^{3+} (Fig. 10C). Most of the iron atoms within the encapsulated domains are not affected by slow passivation to air at 298 K, as the thickness of the oxide skin formed at the periphery of these crystallites may be on the order of 1.5 to 5 monolayers (*37*), or alternatively, some metallic regions may not be able to communicate with the gas phase under these conditions. In addition to these two mechanisms, it is also expected that some of the Fe^{3+} and Fe^{2+} components detected in this study compose a stable interfacial state between negatively charged clay layers and metallic iron domains; however, since these atoms provide only a small fraction of the total Fe^{2+} and Fe^{3+} components, we have not included them in this discussion.

Stability of metallic domains to redox cycles. Metallic iron particles formed within reduced 75/25 Fe/Al-PILC are believed to be in the form of "pancake-shaped" islands with a large fraction of iron atoms exposed to the gas phase as shown in Fig. 9B. The fact that all of the metallic component can be oxidized to Fe^{3+} during the slow passivation treatments (see Fig. 9C) provides evidence that these iron islands are indeed "thin" and exposed to the gas phase. The morphology of these particles is inferred from the relatively intact nature of the clay structure (viz., BET, XRD) and the remarkable ability to oxidize and reform them in a reversible fashion in the apparent absence of sintering (Fig. 3 and Table 1). Since it is generally recognized that iron particles supported on silica do not wet the surface (*38*), the thin and accessible nature of these crystallites appears to be related to the presence of the layered clay structure.

The hyperfine field of reduced 75/25 Fe/Al-PILC (ca. 308–305 kOe) is about 10 kOe smaller less than that obtained from reduced 100 Fe-PILC. This decrease may be due to the presence of smaller metallic domains. An alternate explanation may be that a greater fraction of metallic iron domains is subject to a surface distribution of hyperfine fields and/or contains greater amounts of nonmagnetic impurities in a manner which decreases the effective magnetization of these domains.

Synthesis of Oxidized Iron Domains

The reduction mechanism which creates iron oxide particles in the 10 to 40 nm size range observed by TEM is difficult to explain. It seems that these particles are formed by a massive nucleation/migration of iron oxide pillars rather than a subsequent oxidation of metallic domains. In the absence of reduction-resistant aluminum pillars, iron oxide pillars are believed to be less encumbered to migrate and coalesce within the interlayer space. The massive nucleation and growth of three-dimensional particles (TEM) are expected to cleave some clay layers and may cause some encapsulation of these domains as well (see Figs. 9B and 10B).

The hypothesis noted above is supported by the fact that formation of large iron oxide particles becomes less apparent as the concentration of discrete aluminum pillars increases and the concentration of iron pillars decreases. For clays containing discrete aluminum pillars, the pillared structure is stabilized as a result of strong bonding between the clay surface and the aluminum oxide pillars (*2*). This structure is expected to inhibit growth of iron oxide pillars into three-dimensional crystallites of either reduced or oxidized iron. This behavior may be attributed to (i) a "jello mold" effect provided by the clay layers located above and below the iron oxide pillars, (ii) a decrease in the amount of iron oxide exchanged into the interlayer region compared to the amount of aluminum oxide, and (iii) an inhibition of iron transport provided by the "diluting" influence of increased numbers of aluminum oxide pillars.

The discrete nature of iron oxide domains and metallic iron appears justified on the basis of the observation that Mössbauer studies of reduced 50/50 Fe/Al-PILC, in the absence of platinum, show no signs of metallic iron formation even though a small number of the iron oxide particles are observed via TEM (Table 3). Moreover, it is expected that if metallic iron were formed exclusively at the exterior of iron particles, for example, then these metal atoms would show a high degree of oxidation following passivation in air. Alternatively, formation of reduced iron domains within larger iron oxide particles run contrary to the "hydrogen driving force" applied to these crystallites during reduction.

Iron Decoration of Aluminum Pillars

On the basis of the preparation procedures discussed earlier, 1 discrete aluminum oxide pillar is expected for every 1.4 discrete iron oxide pillars in 50/50 Fe/Al-PILC. The relatively high concentration of aluminum oxide pillars in 50/50 Fe/Al-PILC may provide a larger "sink" for iron oxide pillars to interact/react with aluminum oxide pillars. In order to form a $(3.0\ \text{nm})^3$ metallic iron particle, ca. 2289 iron atoms, equivalent to 763 $Fe_3(OH)_4^{5+}$ pillars, are required. For 50/50 Fe/Al-PILC, iron-containing species must migrate from/through a network of 545 aluminum oxide pillars to form a metallic domain. For 75/25 Fe/Al-PILC, the number of aluminum pillars affecting the same migration iron is only 182.

It is noteworthy that a large fraction of iron in 50/50 Fe/Al-PILC can be reduced to Fe^{2+} at 423 K (i.e., low temperatures) in the presence of platinum (ca. 80.4%), but once in this state, undergoes little additional reduction at temperatures as high as 673 K. These data run contrary to the behavior of the other specimens examined and appear to support the concept that reaction/mixing occurs between iron species and the sur-

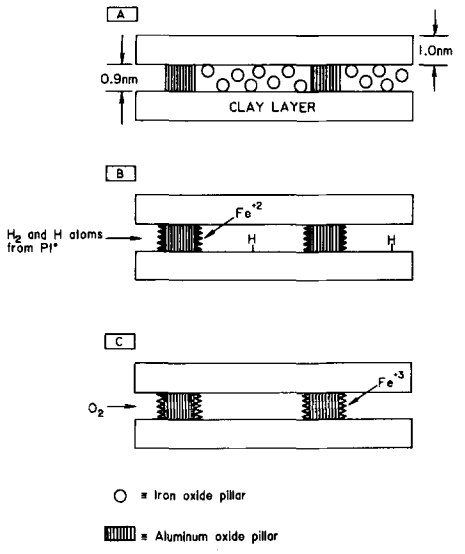

FIG. 11. Schematic representation of 50/50 Fe/Al-PILC: (A) as prepared after freeze-drying, (B) Fe^{2+} decoration onto aluminum oxide pillars after reduction in 101 kPa of hydrogen for 2 h at 423–723 K, and (C) complete oxidation back to Fe^{3+} after slow passivation for 12 h in 21 kPa of oxygen at 298 K.

faces of the aluminum oxide pillars (Figs. 11A and 11B).

Calculations indicate that if little agglomeration of aluminum oxide pillars occurs in 50/50 Fe/Al-PILC specimens, there should be sufficient surface area on the aluminum oxide pillars to accommodate about 90% of the iron pillars. Since iron and iron oxides are known to be more weakly accommodated on silica than on alumina, it appears that at least one monolayer of iron may preferentially decorate the surfaces of the aluminum oxide pillars (Figs. 11B and 11C). The decorated iron is stabilized as Fe^{2+} and slow passivation of these specimens results in total reoxidation to Fe^{3+}, consistent with a highly dispersed Fe^{2+} phase. Because little or no metallic iron is generated in this specimen, it appears that aluminum oxide surfaces must be well-titrated with Fe^{2+} prior to the formation of metallic iron. Also, since little Fe^{2+} is generated in the absence of platinum, it appears that hydrogen atom spillover from platinum to nearby silica-clay layers may provide a key ingredient for iron decoration.

Effects of Platinum Addition

Platinum facilitates the reduction of iron in every sample tested. For 100 Fe-PILC, the amount of metallic iron increases from 15.5 to 62.8% after platinum addition. For 50/50 Fe/Al-PILC, the formation of a major Fe^{2+} phase and a small amount of metallic iron (ca. 10.3%) is observed only after platinum has been added. Mössbauer spectra of alloy-PILC suggest the formation of a spinel-like structure after reduction in the presence of platinum, and in the case of platinum addition to 100 Fe-PILC, 12.5% of the Fe^{3+} initially present in this sample can be reduced to Fe^{2+} at room temperature!

Mössbauer features attributable to Fe–Pt alloys are not observed during reduction of any of the aforementioned samples. Also, the general trends observed in the Fe^{3+} and Fe^{2+} quadrupole splittings are not significantly influenced by platinum impregnation when compared to platinum-free specimens at similar levels of reduction. Therefore, it appears likely that iron clusters containing Fe^0, Fe^{2+}, or Fe^{3+} are not in intimate contact with platinum. Hydrogen spillover from platinum to the clay surface and subsequent migration to, and reduction of, iron pillars appears responsible for the observed behavior. These results are in general agreement with earlier ESR studies by Sancier and Inami (*39*) who found that reduction of iron oxide on either silica or alumina supports was facilitated by platinum.

SUMMARY/CONCLUSIONS

The results of this study indicate the feasibility of preparing both alloy-pillared and mixed pillared clays. The stability and sinter-resistant nature of reduced iron domains formed within the framework supplied by mixed pillared precursors appears to provide a good means for preparing and stabilizing small iron crystallites. These crystallites, coupled with the shape-selective nature of the support and its apparent

thermal stability in redox environments to 723 K, provide a unique set of physical characteristics with potential catalytic applications. Iron can preferentially decorate the surfaces of aluminum oxide pillars contained within the structure with chemical treatments involving hydrogen atoms providing a key ingredient in this process.

ACKNOWLEDGMENTS

Support for this work from the Auburn University Space Power Institute as funded by the SDIO Innovative Science and Technology Office and the Defense Nuclear Agency under Contract 001-85-C-0183 is acknowledged. We also thank Mr. Rex Sherwood and Drs. Carl Lund and Terry Baker at the Exxon Corporate Research Science Laboratories for assistance during CAEM studies.

REFERENCES

1. Brindley, G. W., and Sempels, R. E., *Clay Miner.* **12,** 229 (1977).
2. Lahav, N., Shani, U., and Shabtai, J., *Clays Clay Miner.* **26,** 107 (1978).
3. Vaughan, D. E. W., Lussier, R. J., and Magee, J., U.S. Patent 4,176,090 (1979).
4. Leoppert, R. H., Mortland, M. M., and Pinnavaia, T. J., *Clays Clay Miner.* **27,** 201 (1979).
5. Endo, T., Mortland, M. M., and Pinnavaia, T. J., *Clays Clay Miner.* **28,** 105 (1980).
6. Endo, T., Mortland, M. M., and Pinnavaia, T. J., *Clays Clay Miner.* **29,** 153 (1981).
7. Shabtai, J., U.S. Patent 4,238,364 (1980).
8. Vaughan, D. E. W., and Lussier, R. J., "Proc. 5th Inter. Conf. Zeolites" (L. V. Rees, Ed.), pp. 94–101. Heyden, London, 1980.
9. Occelli, M. L., and Tindwa, R. M., *Clays Clay Miner.* **31,** 22 (1983).
10. Vaughan, D. E. W., and Lussier, R. J., U.S. Patent 4,271,043 (1981).
11. Pinnavaia, T. J., and Raythatha, R. H., U.S. Patent 4,629,712 (1986).
12. Lee, W. Y., M.S. thesis, Auburn University, 1987.
13. Baker, R. T. K., *Catal. Rev. Sci. Eng.* **19,** 161 (1979).
14. Rozenson, I., and Heller-Kallai, L., *Clays Clay Miner.* **25,** 94 (1977).
15. Cardile, C. M., and Johnston, J. H., *Clays Clay Miner.* **34,** 307 (1986).
16. Rozenson, I., and Heller-Kallai, L., *Clays Clay Miner.* **24,** 271 (1976).
17. Tzou, M. S., Ph.D. dissertation, Michigan State University 1983.
18. Mørup, S., Clausen, B.S., and Tøpsoe, H., *J. Phys. C* **6,** 287 (1976).
19. Mørup, S., Dumesic, J. A., and Tøpsoe, H., "Applications of Mössbauer Spectroscopy" (R. Cohen, Ed.), Vol. 2. Academic Press, New York, 1980.
20. Shinjo, T., Hine, S., and Takada, T., "Proc. 7th Inter. Vac. Congr. & 3rd Inter. Conf. Solid Surfaces (Vienna)," p. 2655. 1977.
21. Shinjo, T., Matsuzuwa, T., Mizutani, T., and Takeda, T., *Japan J. Appl. Phys. Suppl.* **2,** 729 (1974).
22. Violet, C. E., and Lee, E. L., "Mössbauer Effect Methodology" (I. J. Gruverman, Ed.), Vol. 2, pp. 171–179. Plenum, New York, 1966.
23. Duncan, S., Owens, A. H., Semper, R. J., and Walker, J. C., *Hyperfine Interactions* **4,** 886 (1978).
24. Keune, W., Lauer, J., Gonser, U., and Williamson, D. L., *J. Phys. C* **2,** 69 (1979).
25. Boudart, M., Delbouille, A., Dumesic, J. A., Khammounma, S., and Tøpsoe, H., *J. Catal.* **37,** 486 (1975).
26. Fugimoto, K., and Boudart, M., *J. Phys. C* **2,** 81 (1979).
27. Lee, J. B., *J. Catal.* **68,** 27 (1981).
28. Garten, R. L., "Mössbauer Effect Methodology" (I. J. Gruverman and C. W. Seidal, Eds.), Vol. 10, p. 69. Plenum, New York, 1976.
29. Bartholomew, C. H., and Boudart, M., *J. Catal.* **29,** 278 (1973).
30. Vaishava, P. P., Ktorides, P. I., Montano, P. A., Mbadcam, K. J., and Melson, G. A., *J. Catal.* **96,** 301 (1985).
31. Dickson, B. L., and Smith, G., *Canad. Mineral.* **14,** 206 (1976).
32. Garten, R. L., and Ollis, D. F. *J. Catal.* **35,** 232 (1974).
33. Hobson, M. C., and Gager, H. M., "Proceedings, 4th International Congress on Catalysis, Moscow, 1968" (B. A. Kazansky, Ed.), p. 48. Adler, New York, 1968.
34. Hobert, H., and Arnold, D., "Proc. Conf. Appl. Mössbauer Effect, Hungary," p. 325. 1969.
35. Johansson G., *Acta Chem. Scand.* **14,** 771 (1960).
36. Kundig, W., Ando, K. J., Lindquist, R. H., and Constabairs, G., *Czech. J. Phys. B* **17,** 467 (1967).
37. Suzdalev, I. P., and Amulyavichus, A. P., *Sov. Phys. JETP* **36,** 929 (1973).
38. Hobson, M. C., *Prog. Surf. Membr. Sci.* **5,** 1 (1972).
39. Sancier, K. M., and Inami, S. H., *J. Catal.* **11,** 135 (1968).